A coupling strategy based on anisotropic mesh adaptation for solving two- fuid fl ows

Thi Thu Cuc Bui, Pascal Frey, Bertrand Maury

INTERNATIONAL JOURNAL FOR NUMERICAL METHODS IN FLUIDS
Int. J. Numer. Meth. Fluids 2009; **x**:1–10 *Prepared using* fldauth.cls *[Version: 2002/09/18 v1.01]*

A coupling strategy based on anisotropic mesh adaptation for solving two-fluid flows

C. Bui[1,*], P. Frey[1,2] and B. Maury [3]

[1] *UPMC Univ Paris 06, UMR 7598, Laboratoire J.L. Lions, F-75005 Paris, France*
[2] *Universidad de Chile, UMI 2807, Centro de Modelamiento Matemático, Santiago, Chile*
[3] *Université Paris Sud, Laboratoire de Mathématiques, 91405 Orsay Cedex, France*

SUMMARY

We propose a coupling strategy for solving efficiently bifluid flows based on the Stokes equations. Our approach relies on a level set formulation of the interface capturing problem, and involves a finite element discretization for the fluid resolution, the method of characteristics for solving the advection of the interface and the anisotropic mesh adaptation of the computational domain in the vicinity of the interface for better accuracy. Copyright © 2009 John Wiley & Sons, Ltd.

KEY WORDS: two-fluid flows; mesh adaptation; Stokes equation; advection; level sets

1. INTRODUCTION

The numerical resolution of multifluid problems with interfaces requires the accurate discretization and tracking of the natural interface separating two immiscible fluids. Indeed, in many such fluid flows, the physical time scale and length scales are so small that reliable experiments and observations are almost impossible. Hence, in the last resort, numerical modelling appears to be the only alternative to investigate and sometimes to understand physical phenomena. One of the major challenge in this context is to deal with the evolution of the interface and the induced changes of its geometry and topology. However, several difficulties may jeopardize the numerical resolution of the problem. Firstly, interfaces are mostly characterized by large jumps of viscosity and density between the fluids that must be properly taken into account and resolved to satisfy momentum balance in this area. Mass conservation is also especially important in interfacial flows. Furthermore, the surface tension force must be considered in the model and accurately evaluated. And finally, the resolution

*Correspondence to: Thi Thu Cuc Bui, UPMC Univ Paris 06, UMR 7598, Laboratoire J.L. Lions, F-75005 Paris, France.

Contract/grant sponsor: The first author is supported by a PhD scholarship from the French Centre National de la Recherche Scientifique.

of the interface must be preserved at all stages, even in the extreme cases of folding, merging and breaking, and more generally all topology changes.

Since the seminal work of Harlow and Welch [37], numerous methods have been proposed to address the problem of interfacial flows (to get an overview of the literature devoted to this topic, see the comprehensive surveys [4, 19, 52, 53], among others). Regarding the classification of numerical methods, a simple yet conventional way is to subdivide the algorithms for fluid flows into two classes, depending on whether a moving mesh is used or not:

1. On the one hand, Lagrangian or Arbitrary Lagrangian Eulerian methods (see e.g. [22] and references therein) are designed to follow the interface evolution using a set of markers and actually deform the discretization grid. In the Lagrangian setting, each grid cell contains the same fluid part throughout the whole computation, whereas the ALE framework allows to relax the vertex-fluid particle identification, which reduces mesh distorsion. These approaches are known to face difficulties in handling interface markers when the interface becomes highly stretched or distorded and the changes of topology are always extremely difficult to manage. Some recent developments in front-tracking methods have overturned previous drawbacks and allow interfaces to merge [56, 51].
2. On the other hand, the alternative consists in introducing a scalar valued level set function to define the interface manifold, and such techniques are usually described as Eulerian techniques. The first work on this topic shall probably be credited to Dervieux and Thomasset [20]. These approaches are characterized by a fixed coordinate system and the fluid travels from one grid cell to another. Although topology changes are easily handled, poor mass conservation is a real concern with the level set methods [54]. To improve this aspect, level set techniques can be coupled with conservative methods [26]. Here, the interface is *captured*, *i.e.*, it is explicitly discretized from the properties of the field density variable and the level set function. Namely, the interface is represented as the zero level set of a distance function. The advantage of this approach is that the level set function that defines the interface propagates with the fluid and thus obeys a simple transport equation, *i.e.,* is convected by the velocity field solution to the fluid equations. Another advantage of this interface-capturing approach is that suitable expressions of the interface normal and curvature can be computed from the level set function (see the book by Sethian [48] and references therein).

Based on these considerations, we have set our numerical modeling strategy in the context of Eulerian and interface-capturing methods. But at the difference of others that use a fixed structured grid during the simulation, here we rely heavily on mesh adaptation using unstructured anisotropic triangulations. Our choice is notably motivated by the following arguments and reasons:

(i) the explicit interface-capturing technique allows to deal with complex interfacial motions and topology changes;
(ii) the flow resolution is decoupled from the advection part;
(iii) the anisotropic mesh adaptation, based on the geometric properties of the interface and the physical properties of the fluid, answers to the need for an accurate representation of the interface with a minimal number of unknowns;
(iv) the resolution of the flow equations between two viscous immiscible fluids needs accounts for large viscosity ratios between the fluids;

(v) the advection term is treated by using a Lagrangian tracking algorithm along characteristic lines combined with a Galerkin finite element scheme, while maintaining the convenience and efficiency of a fixed adapted computational mesh and relaxing the CFL condition.

In addition, we have chosen the finite element method for the spatial discretization as it assumes the minimal regularity for the existence and the uniqueness of a solution and it is especially well-suited for mesh adaptation based on *a posteriori* error estimates. We will show also that fluid coalescence and detachment can be efficiently treated with the sharp interface definition, such situations proscribing actually the use of a diffuse interface.

The paper is organized as follows. In Section 2, the main theoretical aspects of our numerical coupling strategy are described. In Section 2.1, we introduce the continuous model of fluid flow between two fluids of different properties and we present the Stokes equations. In Section 2.2, the level set formulation of this problem is described in the context of interface capturing. The variational formulation and the finite element discretization are outlined in Section 2.3 and 2.4, respectively. Section 2.5 concerns the approximation of the surface tension term on unstructured triangulations. The Uzawa algorithm for solving the linear system is briefly reviewed in Section 2.6 and some enhancements are proposed to deal with large viscosity ratios. Section 2.7 is devoted to mesh adaptation based on an anisotropic metric tensor defined at mesh vertices. The advection of the level set is treated by means of a Galerkin finite element scheme and a method of characteristics, described in Section 2.8. The overall coupling scheme is finally presented Section 2.9. The second part of this paper, Section 3, presents several application examples to emphasize the efficiency and reliability of the proposed strategy.

2. THEORETICAL ASPECTS

As mentioned in the introduction, we investigate here the simulation of the unsteady incompressible flow between two viscous Newtonian immiscible fluids of different rheological behaviors. In this model, we deliberately neglect all parameter variations related to the temperature field evolution, the flow is thus treated as isothermal. In addition, we may assume the fluids to be homogeneous, *i.e.,* the density and viscosity functions are considered as constant within each fluid. We consider the interface between the fluids as a manifold of zero thickness endowed with a surface tension of constant coefficient. It is then commonly assumed that viscosity and density are discontinuous across this interface and that there is no mass transfer between the fluids through it [10].

2.1. The model equations

We suppose that the immiscible fluids are confined to an open bounded computational domain Ω of $\mathbb{R}^d$ ($d = 2, 3$). We denote the outer boundary of the domain by Σ (often a rectangular box, in practice), the subdomains occupied by the fluids $\Omega^1(t)$ and $\Omega^2(t)$ and the interface between the fluids by $\Gamma(t)$, such that $\Gamma(t) = \partial\Omega^1(t) \cap \partial\Omega^2(t)$, where $\partial\Omega^i(t)$ is the boundary of $\Omega^i(t)$. The domains Ω^i can have several connected components and the interface $\Gamma(t)$ can possibly intersect the outer boundary Σ (cf. Figure 1) and we suppose that:

$$\overline{\Omega^1}(t) \cup \overline{\Omega^2}(t) = \overline{\Omega} \qquad \text{and} \qquad \Omega^1(t) \cap \Omega^2(t) = \emptyset.$$

We have introduced a time dependency in the notations as the domains Ω^i and the interface Γ are evolving in time.

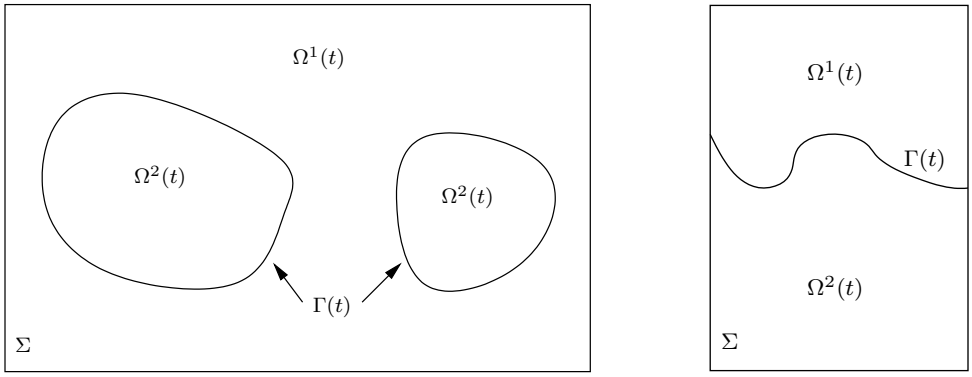

Figure 1. *Example of configurations of bifluid flow computational domains.*

Considering the physical hypothesis we have introduced previously, we shall consider that, at each time step t, the flow of each fluid is then governed by the quasi-static incompressible Stokes equations [49], written in each subdomain Ω^i:

$$\begin{cases} -\mu^i \Delta \mathbf{u}^i + \nabla p^i = \rho^i \, \mathbf{f}^i \\ \qquad\qquad \operatorname{div} \mathbf{u}^i = 0 \end{cases} \tag{1}$$

where $\mathbf{u}^i(\mathbf{x}, t)$ is the velocity of fluid, $p^i(\mathbf{x}, t)$ is the pressure, ρ^i and μ^i are the density and the dynamic viscosity of each fluid, respectively and $\mathbf{f}$ is an external force exerted on the fluid, $\mathbf{f} = \mathbf{f}^i$ in $\Omega^i(t)$. The unknown velocity and pressure functions are of the form $\mathbf{u} = \mathbf{u}^i$ and $p = p^i$ in $\Omega^i(t)$, $i = 1, 2$. Notice that there is no temporal derivative in this equation. Physically however, this does not means that the flow is steady. This only reflects that the forces exerted on the fluid are in a state of dynamic equilibrium as a result of a rapid diffusion of the momentum. Hence, the transient character of the solution is related to the motion of the two fluids and of the interface.

We have assumed that the surface tension effect must be taken into account at the interface. Therefore, this system is endowed with conditions on the continuity of the velocity and on the balance of the normal stress with the surface tension across the interface $\Gamma(t)$:

$$\begin{cases} \qquad \mathbf{u}^1 - \mathbf{u}^2 = \mathbf{0} \\ (\sigma^1 - \sigma^2) \cdot \mathbf{n}^1 = -\gamma \, \kappa \, \mathbf{n}^1 \end{cases} \tag{2}$$

where $\sigma = \mu(\nabla \mathbf{u} + (\nabla \mathbf{u})^t) - p \, \mathbf{I}$ denotes the stress tensor, $\mathbf{n}^1$ is the unit exterior normal vector to $\Gamma(t)$ of $\Omega^1(t)$ pointing from $\Omega^1(t)$ to $\Omega^2(t)$ (we assume that $\Gamma(t)$ is sufficiently smooth), $\gamma > 0$ is the surface tension coefficient assumed to be constant along the interface, κ is the signed mean curvature of the interface, being positive if the curve bends towards $\Omega^1(t)$ and negative otherwise. These equations can be completed with some usual Dirichlet, Neumann or mixed boundary conditions on Σ:

$$\mathbf{u} = \mathbf{u}_D \text{ on } \Sigma_D, \quad \sigma \cdot \mathbf{n} = \mathbf{s}_N \text{ on } \Sigma_N, \quad \Sigma_D \cup \Sigma_N = \partial\Omega, \quad \Sigma_D \cap \Sigma_N = \emptyset. \tag{3}$$

An initial condition is also considered:

$$\Gamma(0) = \Gamma^0 \tag{4}$$

where Γ^0 is the initial position of the interface and indicates the initial shape of each subdomain $\Omega^i(t)$. For the sake of simplicity, we will now omit the time dependency and write simply Ω^i and Γ instead of $\Omega^i(t)$ and $\Gamma(t)$, respectively.

2.2. Level sets and interface capturing

The principal difficulty in evolving interfaces is the correct handling of geometry and topology changes. To overcome this difficulty, the problem can be reformulated on a fixed computational domain using the level set function. Here, following Osher and Sethian [43] (see also [48]), we introduce the signed distance function to the interface $\Gamma(t)$, as follows:

$$\phi(\mathbf{x}, t) = \pm \min_{\mathbf{y}\in\Gamma(t)} \|\mathbf{x} - \mathbf{y}\| \tag{5}$$

where the function ϕ is taken positive in $\Omega^1(t)$ and negative in $\Omega^2(t)$. Hence, at each time step t, the fluid interface corresponds to the zero isocontour of the continuous function ϕ:

$$\Gamma(t) = \{\mathbf{x} \in \Omega \,:\, \phi(\mathbf{x}, t) = 0\}\,. \tag{6}$$

We use here the approach suggested by Sussman et al. [54] for the incompressible two phase flows. The interface between the two fluids is then captured at each time step t by advecting the level set function ϕ with the flow velocity $\mathbf{u}$, *i.e.,* solving the Cauchy problem:

$$\begin{cases} \dfrac{\partial \phi}{\partial t}(\mathbf{x}, t) + \mathbf{u}(\mathbf{x}, t) \cdot \nabla \phi(\mathbf{x}, t) = 0, & \forall\, (\mathbf{x}, t) \in \Omega \times \mathbb{R}^+ \\ \phi(\mathbf{x}, 0) = \phi^0(\mathbf{x}), & \forall\, \mathbf{x} \in \Omega \end{cases} \tag{7}$$

where $\phi^0(\mathbf{x})$ is the signed distance function to Γ^0.

At each time step, several quantities need to be updated and then substituted in the Stokes equations (1), (2). The density and the viscosity are constant in each fluid and take different values depending on the sign of the level set function and hence we can define on Ω:

$$\rho = (\rho^1 - \rho^2) H(\phi) + \rho^2\,, \quad \text{and} \quad \mu = (\mu^1 - \mu^2) H(\phi) + \mu^2\,, \tag{8}$$

where H is the Heaviside function. In the level set framework, the unit normal vector $\mathbf{n}$ to the interface and the mean curvature κ at the interface are usually computed via the function ϕ as:

$$\mathbf{n} = \left.\frac{\nabla \phi}{|\nabla \phi|}\right|_{\phi=0} \qquad \text{and} \qquad \kappa = \operatorname{div} \mathbf{n} = \operatorname{div} \left.\left(\frac{\nabla \phi}{|\nabla \phi|}\right)\right|_{\phi=0}. \tag{9}$$

However, we will see below another geometric technique to approximate $\mathbf{n}$ and κ, that revealed less sensitive to numerical artifacts.

2.3. The variational formulation

To simplify the writing and without loss of generality, we shall deal here with homogeneous Dirichlet boundary conditions. At the initial time, the interface is smooth and we can reasonably assume it remains sufficiently smooth over a time period T. We consider in this

section the instantaneous Stokes problem for a given time t, at which we assume that the interface is regular (C^2). We use a standard notation for Sobolev spaces and we consider the functional spaces:

$$X = H_0^1(\Omega)^d, \quad V = \{\mathbf{v} \in X : \operatorname{div} \mathbf{v} = 0\}, \quad M = L^2(\Omega) \tag{10}$$

for the test functions, the velocity and the pressure, respectively and we observe that the transmission condition on the interface involves the stress tensor σ, thus the pressure has no indeterminate constant and this justifies the choice of the pressure space M. By denoting

$$A_1(\mathbf{u}) = \nabla \mathbf{u} + (\nabla \mathbf{u})^t,$$

we have the identity $\Delta \mathbf{u} = \operatorname{div} A_1(\mathbf{u})$ in each subdomain Ω^i due to the incompressibility condition $\operatorname{div} \mathbf{u} = 0$. Hence, taking the scalar product in $L^2(\Omega^i)^d$ of the first equation in the Stokes system (1) with a test function $\mathbf{v} \in X$ and summing on i, using Green's formula, we obtain the following equation:

$$\begin{aligned} \sum_{i=1}^{2} \int_{\Omega^i} (\mu^i A_1(\mathbf{u}^i) - p^i I) : \nabla \mathbf{v}^i \, dx + \sum_{i=1}^{2} \int_{\partial\Omega^i} (-\mu^i A_1(\mathbf{u}^i)\mathbf{n}^i + p^i \mathbf{n}^i) \cdot \mathbf{v}^i \, ds \\ = \sum_{i=1}^{2} \int_{\Omega^i} \rho^i \mathbf{f}^i \cdot \mathbf{v}^i \, dx \, . \end{aligned} \tag{11}$$

The symmetry of the operator $A_1(\mathbf{u})$ allows us to write $A_1(\mathbf{u}) : \nabla \mathbf{v} = A_1(\mathbf{u}) : (\nabla \mathbf{v})^t$, which yields the equation:

$$\sum_{i=1}^{2} \int_{\Omega^i} (\mu^i \, A_1(\mathbf{u}^i) - p^i I) : \nabla \mathbf{v}^i \, dx = \sum_{i=1}^{2} \int_{\Omega^i} \frac{1}{2} \, \mu^i \, A_1(\mathbf{u}^i) : A_1(\mathbf{v}^i) \, dx - \int_{\Omega} p \operatorname{div} \mathbf{v} \, dx.$$

Since $\mathbf{v} \in H_0^1(\Omega)^d$ and $\mathbf{n}^2 = -\mathbf{n}^1$ on Γ, the conditions (2) on the interface lead to the following equations:

$$\sum_{i=1}^{2} \int_{\partial\Omega^i} (-\mu^i A_1(\mathbf{u}^i) \, \mathbf{n}^i + p^i \, \mathbf{n}^i) \cdot \mathbf{v}^i \, ds = \int_{\Gamma} (-\sigma_1 \, \mathbf{n}^1 \, \mathbf{v}^1 + \sigma_2 \, \mathbf{n}^1 \, \mathbf{v}^2) \, ds = \int_{\Gamma} \gamma \, \kappa \, \mathbf{v} \cdot \mathbf{n}^1 \, ds.$$

Now, by substituting these two equations in (11), we obtain finally the following variational formulation of the homogeneous problem: *find* $\mathbf{u} \in X$ *and* $p \in M$ *solving*:

$$\begin{cases} \displaystyle\int_{\Omega} \frac{1}{2} \, \mu A_1(\mathbf{u}) : A_1(\mathbf{v}) \, dx - \int_{\Omega} p \operatorname{div} \mathbf{v} \, dx = \int_{\Omega} \rho \, \mathbf{f} \cdot \mathbf{v} \, dx - \int_{\Gamma} \gamma \, \kappa \, \mathbf{v} \cdot \mathbf{n}^1 \, ds \\ \displaystyle\int_{\Omega} q \operatorname{div} \mathbf{u} \, dx = 0 \end{cases} \tag{12}$$

to be satisfied for all $\mathbf{v} \in X$ and all $q \in M$. This problem admits the following equivalent weak formulation: *find* $\mathbf{u} \in X$ *and* $p \in M$ *solving*:

$$\begin{aligned} &\forall \mathbf{v} \in X \, , \qquad a(\mathbf{u}, \mathbf{v}) + b(\mathbf{v}, p) = \ell(\mathbf{v}) \\ &\forall q \in M \, , \qquad b(\mathbf{u}, q) = 0 \, , \end{aligned} \tag{13}$$

where $\ell(\cdot)$ is the linear continuous form defined on X:

$$\ell(\mathbf{v}) = \int_\Omega \rho\,\mathbf{f}\cdot\mathbf{v}\,dx - \int_\Gamma \gamma\,\kappa\,\mathbf{v}\cdot\mathbf{n}^1\,ds\,.$$

The bilinear forms $a(\cdot,\cdot)$ and $b(\cdot,\cdot)$ are defined on $X\times X$ and $X\times M$ by:

$$\begin{cases} a(\mathbf{u},\mathbf{v}) = \displaystyle\int_\Omega \frac{1}{2}\,\mu\,(\nabla\mathbf{u}+(\nabla\mathbf{u})^t) : (\nabla\mathbf{v}+(\nabla\mathbf{v})^t)\,dx\,, \\ b(\mathbf{v},p) = -\displaystyle\int_\Omega p\,\mathrm{div}\,\mathbf{v}\,dx\,. \end{cases} \tag{14}$$

The ellipticity of the form $a(\cdot,\cdot)$ results from the Poincaré-Friedrichs inequality. The following inf-sup condition on the form $b(\cdot,\cdot)$ is usually considered [34]: there exists a constant $\beta>0$, depending only on the geometry of Ω, such that:

$$\forall q\in L^2(\Omega)\,,\qquad \sup_{\mathbf{v}\in H_0^1(\Omega)^d} \frac{b(\mathbf{v},q)}{|\mathbf{v}|_{H^1(\Omega)^d}} \;\geq\; \beta\|q\|_{L^2(\Omega)}\,. \tag{15}$$

As a consequence, for any data $\mathbf{f}$ in $H^{-1}(\Omega)^d$, the problem (1) has a unique solution $(\mathbf{u},p)$ in $H_0^1(\Omega)^d\times L^2(\Omega)$.

2.4. Space discretization

Each subdomain Ω^i is covered by a regular triangulation T_h (see Section 2.7 for the definition of regular), with maximum mesh size h, and such that it is globally a conforming triangulation of Ω, *i.e.* for instance in two-dimensional case, T_h contains a piecewise affine approximation Γ_h of the interface Γ. Under this assumption, every mesh element belongs to a single subdomain Ω^i and this is indeed an interesting feature of our approach.

In a yet classical manner, we approximate each component of the velocity in each element $K\in T_h$ by a polynomial of degree one enriched with a "bubble" function (a polynomial of degree $d+1$ defined as the product of the barycentric coordinates in K with $(d+1)^{(d+1)}$ and vanishing on the faces of K) and the pressure in each element by a polynomial of degree one. Both approximations are continuous accross the element faces except for the pressure at the interface Γ_h. Hence, we consider the following discretizations of the spaces M and V:

$$\begin{aligned} X_h &= \{\mathbf{v}_h\in C^0(\bar\Omega)^d\,;\,\forall K\in T_h,\,\mathbf{v}_h|_K\in(\mathbb{P}_1+b_K)^d\}\cap X \\ M_h &= \{q_h=(q_h^1,q_h^2)\in C^0(\bar\Omega_h^1)\times C^0(\bar\Omega_h^2)\,;\,\forall K\in T_h, q_h|_K\in\mathbb{P}_1\} \\ V_h &= \{\mathbf{v}_h\in X_h\,;\,\forall q_h\in M_h\,,\,\int_\Omega q_h\mathrm{div}\,\mathbf{v}_h\,dx=0\}\,. \end{aligned}$$

The discrete problem relies on the variational formulation (13) and reads: *find* $(\mathbf{u}_h,p_h)$ *in* $X_h\times M_h$ *such that*:

$$\begin{aligned} &\forall\mathbf{v}_h\in X_h\,, && a_h(\mathbf{u}_h,\mathbf{v}_h)+b_h(\mathbf{v}_h,p_h)=\ell_h(\mathbf{v}_h) \\ &\forall q_h\in M_h\,, && b_h(\mathbf{u}_h,q_h)=0\,, \end{aligned} \tag{16}$$

where the forms $a_h(\cdot,\cdot)$, $b_h(\cdot,\cdot)$ and $\ell_h(\cdot)$ are defined by, respectively:

$$\begin{cases} a_h(\mathbf{u}_h, \mathbf{v}_h) = \displaystyle\sum_{K\in T_h} \int_K \frac{1}{2}\,\mu\,(\nabla \mathbf{u}_h + (\nabla \mathbf{u}_h)^t) : (\nabla \mathbf{v}_h + (\nabla \mathbf{v}_h)^t)\,dx\,, \\ b_h(\mathbf{v}_h, p_h) = -\displaystyle\sum_{K\in T_h} \int_K \mathbf{v}_h \cdot \nabla\, p_h\,dx\,, \\ \ell_h(\mathbf{v}_h) = \displaystyle\sum_{K\in T_h} \int_K \rho\,\mathbf{f}\cdot\mathbf{v}_h\,dx - \ell_h^\gamma(\mathbf{v}_h). \end{cases} \tag{17}$$

where $\ell_h^\gamma(\mathbf{v}_h)$ stands for a discrete counterpart of $\int_{\Gamma_h} \gamma\,\kappa\,\mathbf{v}_h\cdot\mathbf{n}^1\,ds$ which will be explicited in the next section.

We denote np and ne the number of points and of elements in T_h. Problem (16) is then equivalent to solving the square linear system:

$$\begin{pmatrix} A & B^t \\ B & 0 \end{pmatrix} \begin{pmatrix} \mathbf{U} \\ P \end{pmatrix} = \begin{pmatrix} F \\ 0 \end{pmatrix} \tag{18}$$

where the matrices $A \in \mathcal{M}_N(\mathbb{R})$ and $B \in \mathcal{M}_{np,N}(\mathbb{R})$, with $N = d(np+ne)$, correspond to the bilinear forms a_h and b_h, respectively, and the vector $F \in \mathbb{R}^N$ corresponds to the right-hand side of the equation. The sparse system (18) is symmetric, but not positive, and its size is equal to dim X_h + dim M_h.

2.5. Approximating the surface tension term

We have mentioned the importance of modeling the surface tension force in interfacial flow simulations. As pointed out in [13], surface tension results in a microscopic, localized surface force that exerts itself on fluid elements at interfaces, in both the normal and tangent directions. In the case of interfaces between fluids, the surface tension contributes a surface pressure that is the normal force per unit interfacial area. Actually, this surface tension balances the normal stress at the interface, according to Equation (2).

Several approaches have been proposed to approximate the surface tension term. This shows that the accurate computation of this term is one of the most critical stage in any interface tracking or capturing technique. Classically, the level set function ϕ is used to calculate the unit normal vector and the mean curvature at the interface using formulas (9). However, this requires a pointwise approximation of the gradient of ϕ and this operation becomes more tedious and error-prone on unstructured triangulations, especially in three dimensions. Therefore, we are looking for an alternate technique.

In our approach, the interface is explicitly discretized in the triangulation T_h, via a set of connected segments (faces in three dimensions) Γ_h. Hence, we shall take advantage of this representation, to design a more straightforward evaluation of surface tension. In [33, 57] for instance, we find an expression for the surface tension at a mesh vertex $\mathbf{x}_i$ of Γ_h that involves only the tangents at the two endpoints of each element adjacent to $\mathbf{x}_i$ in two dimensions (Figure 2). The accuracy of the computation depends then strongly on the evaluation of these tangent vectors, and authors advocated to use a Legendre polynomial fit [57] or a quadratic fit [47] through the point $\mathbf{x}_i$ and the endpoints. In three dimension, a similar expression involves the unit outer normal as well. Here, we propose an alternative to this method, based on the Frénet's formulas for planar (parametric) curves [35].

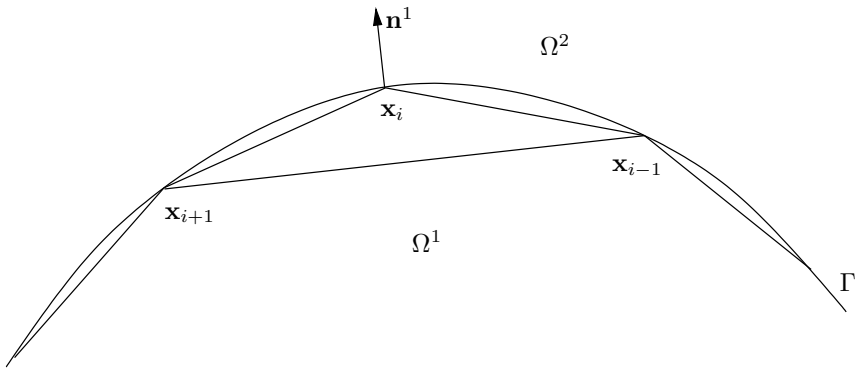

Figure 2. *Example of a geometric discretization of the interface: the Hausdorff distance between the edges and the curve is bounded.*

Without loss of generality, we denote $(\mathbf{x}_i)_{1\leq i\leq ns}$ ($ns < np$) the set of *ordered* vertices of Γ_h, such that $\mathbf{x}_{i-1}, \mathbf{x}_i, \mathbf{x}_{i+1}$ represent three consecutive points along the discrete curve Γ_h. We shall observe that if Γ_h is a closed curve, we have $\mathbf{x}_0 = \mathbf{x}_{ns}$ and $\mathbf{x}_1 = \mathbf{x}_{ns+1}$. Next, we rewrite the surface tension term in Equation (17) using a quadrature formula on each edge $\mathbf{x}_i, \mathbf{x}_{i+1}$ of Γ_h, as follows, for all $\mathbf{v}_h \in X_h$:

$$\begin{aligned} \ell_h^\gamma(\mathbf{v}_h) &:= \sum_{E\subset\Gamma_h} \frac{|E|}{2} \sum_{\mathbf{x}_i\in E} \gamma\,\kappa(\mathbf{x}_i)\,\mathbf{v}_h(\mathbf{x}_i)\cdot\mathbf{n}^1(\mathbf{x}_i) \\ &= \sum_{\mathbf{x}_i\in\Gamma_h} \gamma\,\kappa(\mathbf{x}_i)\,\mathbf{v}_h(\mathbf{x}_i)\cdot\mathbf{n}^1(\mathbf{x}_i) \sum_{\mathbf{x}_i\in E} \frac{|E|}{2}\,, \end{aligned} \tag{19}$$

where E denotes an edge of Γ_h. It remains to be explained how to compute the unit outer normal vector $\mathbf{n}^1$ and the curvature $\kappa(\mathbf{x}_i)$ at each point $\mathbf{x}_i \in \Gamma_h$.

Considering $\mathbf{x}_i \in \Gamma_h$, we define the unit tangent vector $\tau = (\tau_1, \tau_2)^t$ at this point as the unit vector:

$$\tau(\mathbf{x}_i) = \frac{\overrightarrow{\mathbf{x}_{i+1}\mathbf{x}_{i-1}}}{\|\overrightarrow{\mathbf{x}_{i+1}\mathbf{x}_{i-1}}\|}$$

and the unit outer normal $\mathbf{n}^1$ at $\mathbf{x}_i$ is then defined as the unit vector orthogonal to $\tau(\mathbf{x}_i)$, pointing from Ω^1 to Ω^2 (Figure 2):

$$\mathbf{n}^1(\mathbf{x}_i) = (\tau_2(\mathbf{x}_i)\,,\, -\tau_1(\mathbf{x}_i))^t\,.$$

In [30], we introduced the approximation of the local radius of curvature r at $\mathbf{x}_i$ as:

$$r(\mathbf{x}_i) = \frac{1}{4}\left(\frac{\langle\overrightarrow{\mathbf{x}_i\mathbf{x}_{i-1}},\, \overrightarrow{\mathbf{x}_i\mathbf{x}_{i-1}}\rangle}{\langle -\mathbf{n}^1(\mathbf{x}_i),\, \overrightarrow{\mathbf{x}_i\mathbf{x}_{i-1}}\rangle} + \frac{\langle\overrightarrow{\mathbf{x}_i\mathbf{x}_{i+1}},\, \overrightarrow{\mathbf{x}_i\mathbf{x}_{i+1}}\rangle}{\langle -\mathbf{n}^1(\mathbf{x}_i),\, \overrightarrow{\mathbf{x}_i\mathbf{x}_{i+1}}\rangle}\right) \tag{20}$$

and the local curvature $\kappa(\mathbf{x}_i)$ is then classically computed as the inverse of the radius of curvature, *i.e.*, $\kappa(\mathbf{x}_i) = 1/r(\mathbf{x}_i)$, if $\mathbf{n}^1(\mathbf{x}_i)$ is not perpendicular to both $\overrightarrow{\mathbf{x}_i\mathbf{x}_{i-1}}$ and $\overrightarrow{\mathbf{x}_i\mathbf{x}_{i+1}}$, and $\kappa(\mathbf{x}_i) = 0$, otherwise. This technique can be extended straightforwardly to three dimensions, where the unit normal is then taken as the weighted average value of the unit normals of

all triangles sharing vertex $\mathbf{x}_i$ (see [28] for more details on curvature estimation for discrete surfaces).

On a unit test circle, we observed that the discrete curvature value does not oscillate and its approximation is in good accordance with the theoretical value (less than 0.1% deviation). However, numerical artifacts are unavoidable when dealing with complex curves and surfaces, as the information considered is extremely localized. To avoid dramatic changes between the curvatures of adjacent vertices in Γ_h and to reduce noise, we introduced a smoothing procedure on the curvature value. This curvature smoothing is inspired by a Fourier denoising (low-pass filtering) procedure described in [55].

2.6. Solving the linear system

Numerous methods have been proposed to solve the linear system (18). Our ambition to tackle real-life problems rules out the use of direct methods like LU or Choleski decomposition. One alternative consists in dealing with the global system (18), for which a large amount of preconditionners have been proposed (see e.g. [25, 40]). Another alternative relies on eliminating the unknown $\mathbf{U}$, which leads to

$$BA^{-1}B^t\,P = BA^{-1}F\,, \qquad A\,\mathbf{U} = F - B^tP\,. \tag{21}$$

The matrices in the left-hand sides of these equations are still symmetric and a conjugate gradient technique can be employed to solve each problem. As pointed out in [17], the Schur matrix $BA^{-1}B^t$ is likely to behave like a mass matrix for the scalar unknown, which makes this approach quite competitive, as the overall stiffness of the problem finally depends on the condition number of the matrix A only. This condition number is not only related to the discretization of the computational domain Ω, and thus to the triangulation T_h, but it is also closely dependent on the viscosity ratio μ^2/μ^1 between the subdomains. Actually, whereas virtually no problem is noticeable when the two viscosity values are quasi-similar, the resolution of bifluid flows becomes a lot more difficult when the viscosity ratio increases, and even more striking if we consider the simulation of pseudo-rigid particles in a viscous flow. Some strategies have been proposed to overcome this problem (see [15, 2]). In the applications that we propose in this paper, the viscosity ratio does not exceed 100 and thus a simple conjugate gradient with diagonal preconditionning turned out to behave satisfactory.

2.7. Anisotropic mesh adaptation

In order to deal with the discrete fluid problem, we assume that Ω is a polygonal or polyhedral domain in $\mathbb{R}^d$ and we suppose given a triangulation T_h on Ω. Each element K in T_h is a (closed) subdomain of Ω such that $\overline{\Omega} \subset \bigcup_{K\in T_h} K$ and also such that the intersection of any two different elements, if not empty, is reduced to a d-1-simplex (elements cannot overlap). Under these assumptions, we define a *uniform* mesh T_h of Ω as a mesh in which all elements are equally sized and regular (equilateral). A *quasi-uniform* mesh refers then to a mesh for which the ratio of the diameter h_K of an element K in T_h to the diameter ρ_K of its inscribed circle or sphere is bounded by a constant σ independent of h and the variation of its element size is bounded by a constant [18]. As usual, the parameter h characterizes the maximal diameter of elements K in T_h.

Mesh adaptation aims at improving the efficiency and the accuracy of numerical solutions by concentrating more nodes in critical regions, where the solution is not constant and may

change rapidly across neighboring elements, than in other regions of the computational domain. Furthermore, controlling the size, the shape and the orientation of the mesh elements altogether results in even more accurate computations. This control can be achieved by considering a metric tensor field that prescribes the size, the stretching and the orientation of the mesh elements anywhere in the domain. For instance, an anisotropic tensor field can be prescribed by an error indicator or an error estimate (see the papers [5, 8, 27, 23] and the references therein) that relates the approximation error to the element size.

Practically, a symmetric positive definite tensor matrix $M(\mathbf{x})$ is associated with the mesh nodes $\mathbf{x}$ in T_h. From the continuous geometry point of view, elements are characterized by a tensor matrix and thus can be represented by ellipsoids. Hence, size, shape and orientation notions are associated with its volume, the ratios between the lengths of its semi-axes and its principal axis vectors, respectively. Assuming the metric M being prescribed, the aim of the anisotropic mesh generation is to create a quasi-uniform mesh, where the optimal mesh elements are equilateral when their quality is measured in this metric. To this end, we define the measure $|K|_M$ of any element K in T_h with respect to M and its discrete approximation as:

$$|K|_M = \int_K \rho(\mathbf{x}) d\mathbf{x}\,, \quad \rho(\mathbf{x}) = \sqrt{\det(M(\mathbf{x}))}\,, \quad \text{and} \quad |K|_M \approx |K| \sqrt{\det(M(K))}\,, \tag{22}$$

where $M(K)$ is a certain average of $M(\mathbf{x})$ on K and $\rho(\mathbf{x})$ is a density function, often called the adaptation function or the sizing function [39]. The elements in the mesh have then a unitary volume in the metric.

Numerous methods have been developed for generating anisotropic meshes according to a metric tensor. Typical examples are Delaunay based triangulation methods [11, 44, 46], advancing-front methods [32, 41], bubble mesh technique [12, 59] and local mesh modification methods [23, 21]. Most of these methods share in common the definition of the metric tensor based on the Hessian of a solution variable, as primarily suggested by d'Azevedo and Simpson [7] on linear interpolation for quadratic functions on triangles. For instance, given the eigen decomposition of the Hessian of the function u, $H(u) = P\,\mathrm{diag}(\lambda_i)_{1\le i\le d}\,P^t$, we define the metric as suggested in [3, 38]:

$$M = \frac{1}{\varepsilon\,\alpha^2} \frac{|H(u)|}{\max(\mathrm{Cutoff}, |u|)}\,, \quad \text{with} \quad H(u) = P\,\mathrm{diag}(|\lambda_i|)_{1\le i\le d}\,P^t\,, \tag{23}$$

where ε corresponds to the desired interpolation error (typically of the order of 0.01), α is a coefficient on the mesh size, and Cutoff is a safety limit value on the interpolation error.

In the fluid problem we are considering, the interface is defined via the auxiliary level set function ϕ as a zero isocontour of ϕ. We recall that the interface $\Gamma(t)$ is explicitly discretized in the trangulation T_h by a piecewise polygonal curve or surface $\Gamma_h(t)$. In [24], we defined an anisotropic metric M to control the Hausdorff distance between Γ and Γ_h as:

$$M = \frac{\nabla\phi\nabla\phi^t}{h_{min}^2} + \frac{D^2\phi}{\varepsilon}\,, \tag{24}$$

where h_{min} represents the smallest user-specified element size in T_h and ε is such that $d(\Gamma, \Gamma_h) \le \varepsilon$. Endowed with the metric M, the orientation of the elements of T_h will be aligned with the principal directions of curvature and with the normal to Γ and their relative sizes

$h(\mathbf{x})$ will be proportional to the local curvatures by setting $h(\mathbf{x}) = \sqrt{\varepsilon/\kappa(\mathbf{x})}$. Furthermore, this geometric metric associated with the level set function ϕ can be combined with the metric based on the Hessian of the solution using a metric intersection procedure defined in [3].

Given a metric field M, it is natural to define critera to measure how closely the mesh elements are aligned and equidistributed with respect to M. For practical reasons, we introduce an individual measure to evaluate the quality of an element K:

$$Q_{ani}(K) = \alpha_d \, |K|_M \left(\sum_{i=1}^{na} \|e_i\|_M \right)^{-d}, \quad \text{with} \quad \|e_i\|_M = \int_0^1 \sqrt{\langle e_i, M(t) e_i \rangle} dt \,, \tag{25}$$

where e_i is any of the $na = d(d+1)/2$ egdes of the simplex K and α_d is a normalisation constant such that $Q_{ani}(K) = 1$ for a regular element. Notice that $0 \leq Q_{ani}(K) \leq 1$ for all $K \in T_h$ and thus if $Q_{ani}(K)$ is small, then the discrepancy between the element K of the triangulation T_h and the metric specification will be important.

In our strategy, the generation of a quasi uniform mesh is obtained using a Delaunay-based local mesh modification procedure described in three dimensions in [21].

2.8. Advection of the interface

We have mentioned in Section 2.2 that the interface $\Gamma(t)$ is captured at each time step by advecting the level set function ϕ with the flow velocity $\mathbf{u}$, *i.e.*, solving the Cauchy problem (7). Several methods have been proposed to solve this advection equation. However, conventional Galerkin based finite element techniques perform in general poorly on advective transport. Spurious oscillations may occur that jeopardize the accuracy of the solution. Nevertheless, since time and space are linked through the characteristics, we will rely on the method of characteristics (see [45]), combined with a Galerkin finite element approximation on anisotropic meshes. Among the advantages of using the method of characteristics, we are especially interested here in the large time stepping Δt that can be used as no restrictive stability condition on Δt is involved.

Let $\mathbf{X}$ be the characteristic associated to $\mathbf{u}$. Then the characteristic curves of Equation (7), along which $\phi(\mathbf{x}, t)$ remains constant, is solution of the following problem, for all s:

$$\begin{cases} \dfrac{d\mathbf{X}}{dt}(\mathbf{x}, t; s) = \mathbf{u}(\mathbf{X}(\mathbf{x}, t; s), t), \\ \mathbf{X}(\mathbf{x}, s; s) = \mathbf{x}. \end{cases} \tag{26}$$

The point $\mathbf{X}(\mathbf{x}, t; s)$ denotes the position of a fluid particle at the time t that was (or will be) at the position $\mathbf{x}$ at the time s. Given the characteristics computed from Equation (26), the solution to the advection equation is then:

$$\phi(\mathbf{X}(\mathbf{x}, t^{n+1}; t^{n+1}), t^{n+1}) = \phi(\mathbf{X}(\mathbf{x}, t^n; t^{n+1}), t^n) \tag{27}$$

where $t^n = n\Delta t$. Thus, by denoting $\mathbf{X}^n(\mathbf{x})$ an approximation of $\mathbf{X}(\mathbf{x}, t^{n+1}; t^n)$, we have:

$$\phi(\mathbf{x}, t^{n+1}) = \phi(\mathbf{X}^n(\mathbf{x}), t^n) \,, \qquad \text{or} \qquad \phi^{n+1}(\mathbf{x}) = \phi^n \circ \mathbf{X}^n(\mathbf{x}) \,, \tag{28}$$

where $\phi^n(\mathbf{x}) = \phi(\mathbf{x}, t^n)$. At each time t^n, we consider a quasi uniform triangulation T_h^n of the domain Ω, refined in the vicinity of $\Gamma(t^n)$, and a function $\phi^n(\mathbf{x})$ is defined.

We approximate the function ϕ in each element K of T_h^n by a polynomial of degree one, hence we are considering the sequence of spaces W_h^n, for all n:

$$W_h^n = \{\phi_h \in C^0(\bar{\Omega}_h)\,;\, \forall K \in T_h^n\,,\, \phi_h|_K \in \mathbb{P}_1\}\,.$$

Using the basis functions $(\varphi_j)_{1\leq j\leq np}$ of W_h^n, the projection ϕ^{n+1} of the function ϕ on the triangulation T_h^n can be expressed as:

$$\phi^{n+1}(\mathbf{x}) = \sum_{j=1}^{np} \phi^{n+1}(\mathbf{x}_j)\,\varphi_j(\mathbf{x})\,, \tag{29}$$

where np is the number of vertices of T_h^n and $(\mathbf{x}_j)$ representing the set of mesh vertices. Multiplying both sides of (28) by φ_i and integrating over Ω, leads to a linear system of the form:

$$M\Phi = b$$

where the unknown vector Φ is defined as $\Phi = (\phi^{n+1}(\mathbf{x}_i))_{1\leq i\leq np}$, $M = (m_{ij})$ is the symmetric mass matrix:

$$m_{ij} = \int_\Omega \varphi_i(\mathbf{x})\varphi_j(\mathbf{x})\,dx = \sum_{K\in T_h^n} \int_K \varphi_i(\mathbf{x})\varphi_j(\mathbf{x})\,dx$$

and $b = (b_i)$ is the right-hand side:

$$b_i = \int_\Omega \phi^n \circ \mathbf{X}^n(\mathbf{x})\varphi_i(\mathbf{x})\,dx = \sum_{K\in T_h^n} \int_K \phi^n \circ \mathbf{X}^n(\mathbf{x})\varphi_i(\mathbf{x})\,dx\,.$$

In two dimensions of space, we use the following quadrature formula to calculate the integral term in b:

$$\int_K \phi^n \circ \mathbf{X}^n(\mathbf{x})\varphi_i(\mathbf{x})\,dx \approx \sum_{l=1}^{3} \frac{|K|}{3}\,\phi^n \circ \mathbf{X}^n(\xi_l)\varphi_i(\xi_l)$$

where (ξ_l) are 3 Gaussian points in triangle K. However, since the time step Δt is not small, the approximation of the curve $\{\xi_l, \mathbf{X}^n(\xi_l)\}$ using a straight line is obviously not accurate. Actually, we use a piecewise affine discretization to approximate the curve $\{\xi_l, \mathbf{X}^n(\xi_l)\}$ where each segment corresponds to a smaller time step *tol* and a fourth-order Runge-Kutta (RK4) scheme is implemented to solve the ODE (26) on each segment, [16].

Figure 3 presents an example of the resolution of the advection equation (7) for a slightly modified version of the well-known Zalesak slotted disk [60]. Here, the computational domain is $\Omega = [-1, 1] \times [-1, 1]$, the disk of radius 0.2 is centered at $(0, 0.5)$, the width of the slot is 0.04 and the maximum width of the lower bridge, that connects two parts of the disk, is 0.2. The constant angular velocity is set to 1, so the slotted disk shall return to its initial position after a 2π revolution, expecting no change in the interface and on the volume.

Our strategy consists in defining a signed level set function on the initial mesh that is then advected using the method of characteristics with a RK4 scheme. At each time step, the solution of Problem (26) is computed on an anisotropic mesh adapted to the level set function, *i.e.* refined in the vicinity of the zero isocontour. On Figure 3 (right), one can see the refinement of the mesh T_h^{n+1} that accounts for the interface position at times t^n and t^{n+1}. Actually, the problem is solved 4 times on a mesh adapted to both the initial and final positions

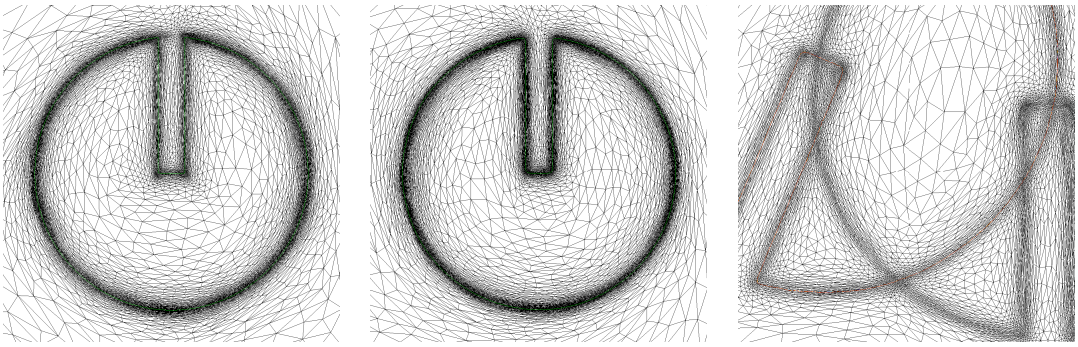

Figure 3. *Zalesak slotted disk test: zoom on the initial mesh (left), the final mesh (center) and closer zoom of the "doubly adapted" mesh at iteration* 9. *The location of the interface is shown using a green or red line.*

of the interface in the period $[t^n, t^{n+1}]$. This procedure allows to use a large time step, here $\Delta t = \pi/8$ (a complete revolution is accomplished in 16 iterations only), much larger than the time step prescribed by the restrictive stability condition: $\Delta t = 5 \times 10^{-4}$ for an element size $h_{min} = 10^{-3}$.

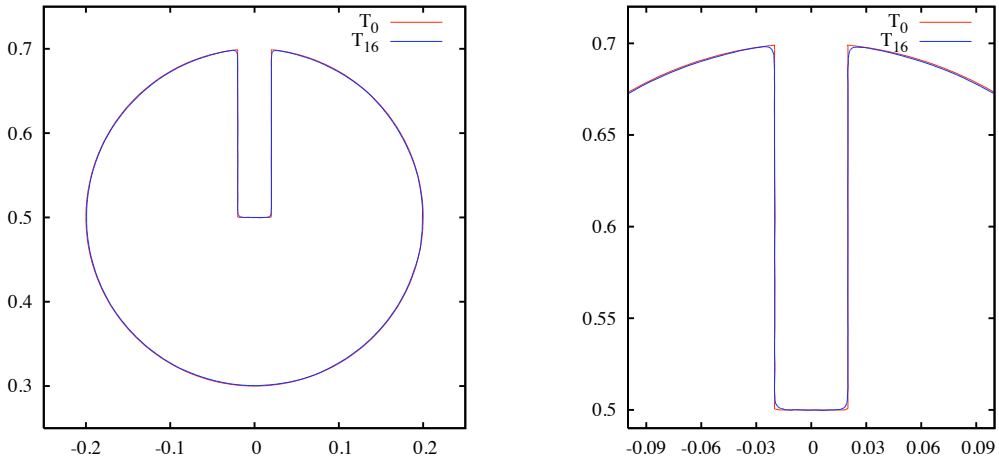

Figure 4. *Zalesak slotted disk test: superposition of the slotted disk (blue line) after one complete revolution and the initial one (red line) and zoom on the sharp corners (right).*

The difference between the slotted disk after one complete revolution and the initial one is showed in Figure 4. To measure the accuracy of the method and to evaluate the loss of mass, we denote by M^n the mass of the slotted disk at a given time step: $M^n = \sum_{K \in T_h^n} S^n(K)$, where $S^n(K)$ represents the area of the part of K where the function ϕ has a non positive value (supposed to define the disk) on the triangulation T_h^n. Then, following [58], we define

two L^1 error measures:

$$E^n = \frac{\left|M^n - M^0\right|}{M^0}, \quad E^{Z,n} = \frac{\sum_K \left|S^n(K) - S^0(K)\right|}{M^0}. \tag{30}$$

The initial mass M^0 is 0.117640, the final mass after one revolution is 0.116981 and the relative errors measured on the final mesh are $E^{16} = 5.59 \times 10^{-3}$ and $E^{Z,16} = 5.97 \times 10^{-3}$, respectively.

2.9. A general coupling strategy

To conclude our presentation, we propose now a general scheme for the coupling strategy as an iterative procedure. At each iteration n, we assume defined a mesh T_h^n for the fluid and a mesh S_h^n for the level set function. Actually, these two conforming finite element meshes do not need to coincide, although the interface at time t^n is explicitly discretized in both meshes with the same accuracy, *i.e.,* corresponding to the same minimal size.

Moreover, in the advection procedure, to compute the solution $(S_h^{n+1}, \phi_h^{n+1})$ at time t^{n+1}, given the solution (S_h^n, ϕ_h^n) at time t^n, we solve the advection equation up to M times: the first $M-1$ times to fully capture the zero isolevel lines at both instances t^n and t^{n+1}, thus to perfectly adapt the mesh in these critical regions, and the last time to actually advect the level set function ϕ_h^n. We found the value $M \geq 3$ suitable in most problems, but this may be context dependent. This adaptation procedure is absolutely necessary, it increases the accuracy of the advection process and it does not impact unfavorably the cpu time.

The overall algorithm is given hereafter.

Given S_h^0 and T_h^0, two meshes locally refined in the vicinity of Γ_h^0.

1. **Initialization** of ϕ_h^0 on S_h^0
2. **Main loop**:
   for each time step $t^n \in [0, T]$:
   - (a) **Resolution** of Stokes's equation: $(T_h^n, \mathbf{u}_h^n)$
   - (b) **Projection** of $\mathbf{u}_h^n$ onto S_h^n: $(S_h^n, \tilde{\mathbf{u}}_h^n)$
   - (c) **Advection loop**:
     for each $k = 1, 2, \ldots, M$
     - i. if $k = 1$, set $S_h^{n,1} = S_h^n$, $\phi_h^{n,1} = \phi_h^n$ and $\tilde{\mathbf{u}}_h^{n,1} = \tilde{\mathbf{u}}_h^n$
     - ii. given $(S_h^{n,k}, \phi_h^{n,k})$ and $\tilde{\mathbf{u}}_h^{n,k}$, solve equation (29), : $(S_h^{n,k}, \tilde{\phi}_h^{n,k+1})$
     - iii. Adapt mesh $S_h^{n,k}$, given $\phi_h^{n,k}$ and $\tilde{\phi}_h^{n,k+1}$: $S_h^{n,k+1}$
     - iv. Project $\mathbf{u}_h^n$ onto $S_h^{n,k+1}$: $\tilde{\mathbf{u}}_h^{n,k+1}$
     - v. If $k < M$ then project ϕ_h^n onto $S_h^{n,k+1}$: $\phi_h^{n,k+1}$
       else project $\tilde{\phi}_h^{n,k+1}$ onto $S_h^{n,k+1}$: $\tilde{\phi}_h^{n+1}$
       goto 2(c)ii, with $k = k + 1$
   - (d) *Renormalization* of $\tilde{\phi}_h^{n+1}$ (optional): $\tilde{\phi}_h^{n+1}$
   - (e) **Adaptation** of $S_h^{n,M+1}$ with respect to $\tilde{\phi}_h^{n+1}$: S_h^{n+1}
     and discretize the interface: Γ_h^{n+1}
   - (f) **Projection** of $\tilde{\phi}_h^{n+1}$ onto S_h^{n+1}: $(S_h^{n+1}, \phi_h^{n+1})$
   - (g) **Adaptation** of S_h^{n+1} to ϕ_h^{n+1} and $\mathbf{u}_h^n$: T_h^{n+1}
3. goto step 2 until $t^n = T$.

The renormalization procedure involved in this algorithm is optional in this context. Its purpose is mainly to maintain the distance property of the level set function ϕ, *i.e.,* to preserve $|\nabla\phi| = 1$ at all times t^n. However, in our approach, only the zero isocontour of ϕ is important as it defines the interface and thus this step could be easily skipped without jeopardizing the numerical resolution. We found it useful only for slightly improving the accuracy of the linear approximation scheme used when splitting the mesh elements intersected by the zero level set curve.

This concludes the theoretical presentation of our approach for solving bifluid flow problems. In the next section, we will provide some application examples for which this coupling strategy was especially very useful and well-suited.

3. APPLICATION EXAMPLES

To emphasize the efficiency and the reliability of our coupling strategy, we present in this section a few application examples in microfluidics, where Stokes models are largely involved. In this type of applications, the surface tension effect must largely be accounted for, although the computation of this term is not our main concern here. All the examples are described in two dimensions and the parameters have been set for the Reynolds numbers to be small $Re \ll 1$, *i.e.,* to belong to the interval $[10^{-4}, 10^{-2}]$, viscous forces dominating advective inertial forces.

Regarding the numerical resolution of the advection equation, the time step must normally be set so as to satisfy a stability condition. Furthermore, due to the explicit discretization of the surface tension term, another restriction is introduced on the time step. For a Stokes flow problem, we found in [31] the following stability criterion, that relates the time step to the ratio between the dynamic viscosity μ and the surface tension coefficient γ:

$$\Delta t_S = c\frac{\mu}{\gamma}h_{min}$$

where h_{min} denotes the minimal element size, and $c \leq 8$ is a constant independent of h_{min}. To this end, in our simulations the internal time step *tol* (see Section 2.8) is chosen as:

$$tol \;\leq\; c\,\frac{\min(\mu^1, \mu^2)}{\gamma}h_{min}\,.$$

3.1. Droplet in micro channel

We present in this section a numerical simulation of the evolution of an elliptic shape droplet in a micro canal. Due to the effect of surface tension, the droplet changes its shape quite quickly toward the stationary shape (that is not a circle due to boundary conditions) and then translate from left to right in the canal. The computational domain is a rectangle of dimensions $l = 200 \times 10^{-6}$ and $L = 800 \times 10^{-6}$ m. The initial droplet shape has a largest diameter of 100×10^{-6} m (in blue on Figure 5). The viscosity of the external (resp. internal) fluid is $\mu^1 = 10^{-2}$ kg/(m·s) (resp. $\mu^2 = 10^{-3}$ kg/(m·s)). Here, we neglect gravitational effects and the surface tension coefficient is taken as $\gamma = 0.001$ N/m.

A Poiseuille flow is assigned on the left inlet, corresponding to a maximal velocity module of 8×10^{-3} m/s, compatible with the boundary condition $\mathbf{u} \cdot \tau = 1.536 \times 10^{-4}$ m/s on the horizontal walls. Finally, a natural Neumann condition $\sigma \cdot \mathbf{n} = 0$ is assigned to the right wall.

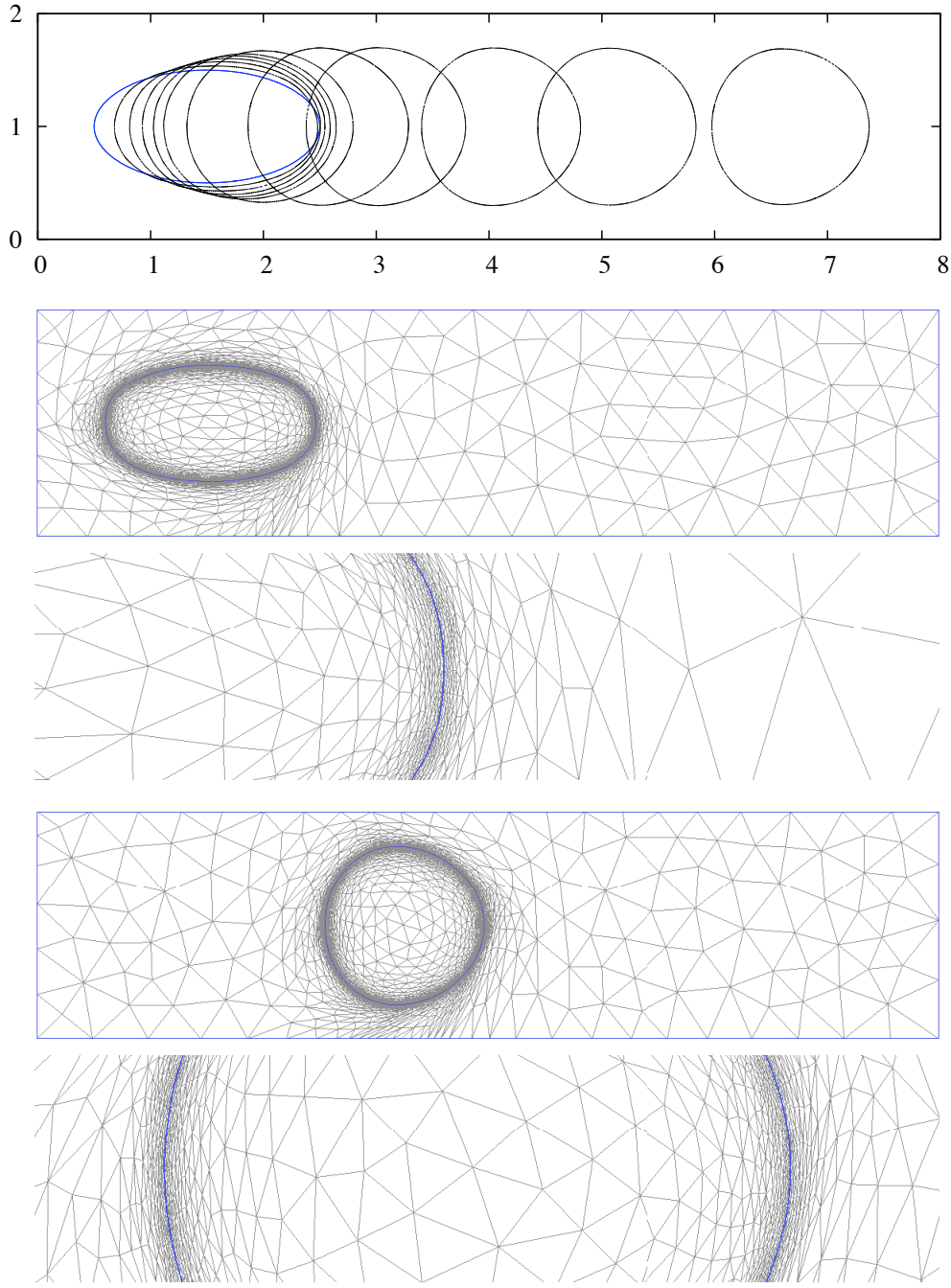

Figure 5. Evolution of an elliptical droplet in a micro channel at various time steps (top) and computational anisotropic meshes adapted to the interface (blue line) at $t = 0.5$ and $t = 25$ ms.

At each time step, the solution is computed on an anisotropic adapted mesh that contains less than $1,200$ vertices, corresponding to a minimal size $h_{min} = 0.2 \times 10^{-6}$ m, *i.e.,* equal to $1/1000$ of the domain section. The maximal anisotropy ratio is about 100. The time step is set to $\Delta t = 0.5$ ms and the internal time step is set to $tol = 0.001$ ms.

3.2. The coalescence of two droplets

Next, we consider here the evolution of two ellipsoidal droplets under the effect of surface tension and their merging into a single drop. The purpose of this example is to emphasize the ability of our approach to handle changes of topology of the interface during its evolution.

This example is largely inspired by an experiment described in [50]. Here, our model consists in two droplets of a viscous fluid ($\mu^2 = 10^{-1}$ kg/(m·s)) embedded in a much lesser viscous fluid ($\mu^1 = 10^{-3}$ kg/(m·s)), in a zero-gravity medium. The surface tension coefficient is $\gamma = 0.03$ N/m. The droplets have an initial elliptic shape whose dimensions have been chosen as follows: the larger drop has semi-axes $a_1 = 0.4$ mm and $b_1 = 0.2$ mm, centered at $(-0.1, 0)$, and the smaller drop $a_2 = 0.23$ mm and $b_2 = 0.15$ mm, centered at $(0.27, 0)$. The initial distance between two droplets is thus 0.02 mm.

The geometry of this problem is symmetric, it would then be natural to solve it in only the half-domain $\Omega^+ = [-0.6, 0.6] \times [0, 0.6]$ (the length unit is 1 mm), imposing a free-slip boundary condition on the symmetry line $y = 0$ and homogeneous Dirichlet boundary conditions on the rest of the domain boundaries. We decided however to solve it on the whole domain

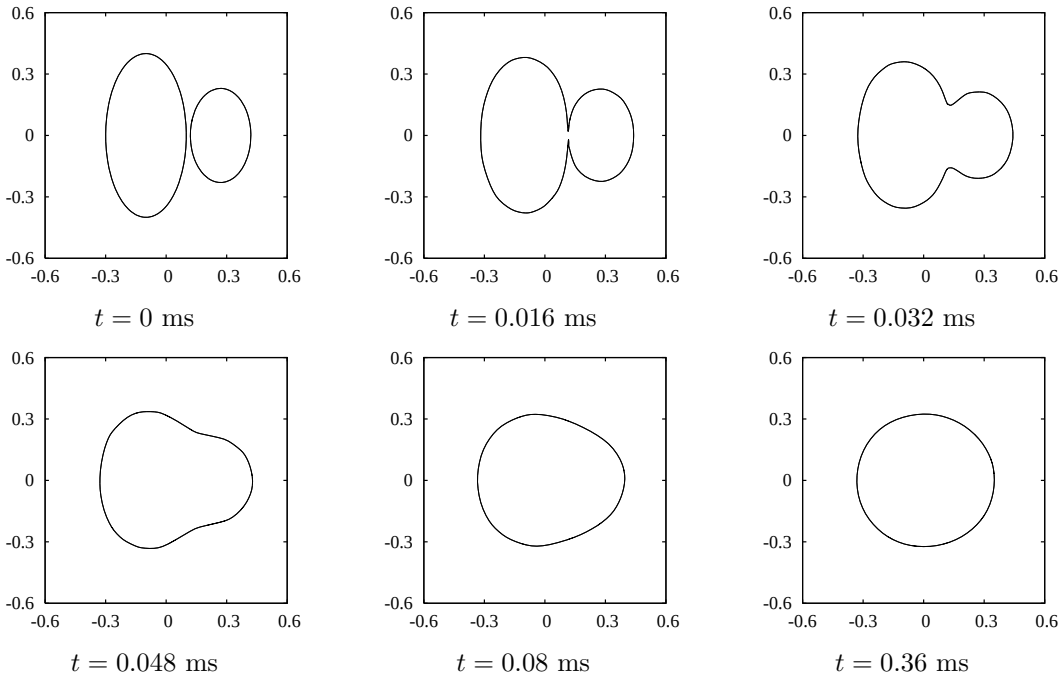

Figure 6. *Coalescence of droplets in zero gravity with a surface tension model: interface development.*

$\Omega = [-0.6, 0.6]^2$ and as we can see on Figure 6, the symmetry is still nicely held during the process. Following the stability condition mentioned previously, the time step is chosen $\Delta t = 0.002$ ms and the substep is $tol = 0.001$ ms.

Obviously, the coalescence is a physical phenomenon that cannot be resolved and simulated with such a simple mathematical model. From the dynamical point of view, the incompressibility makes the fluids hard to coalesce. Using a fix structured mesh can help the coalescence occurs numerically when two zero isocontours arrive in the same cell, it is thus strongly related to the cell size. In our simulations, the minimal size h_{min} is related to the local curvature of the interface and can be very small. Furthermore, in the triangulation T_h, there will always be a mesh node between two closely spaced interfaces (in order to avoid locked elements). This feature may simply prevent the coalescence of bubbles. Nevertheless, we have decided to provoke the fusion in artificial manner. At time $t = 0.016$ ms, instead of considering the zero isocontour as Γ, we considered the isocontour $\phi = \varepsilon$ with $\varepsilon \ll 1$ (in practice $\varepsilon = 2 \times 10^{-4}$), thus resulting in the fusion of droplets (see Figure 6). After the coalescence occured, the simulation resumed and we have considered again the interface as the zero isocontour. The corresponding anisotropic adapted meshes are presented in Figure 7, they correspond to a minimal size $h_{min} = 0.005$ and they all contain less than $1,600$ points.

The initial volume of the discretized droplets is $V_0 = 0.358937$ (the exact value is close to 0.359712), corresponding approximately to the volume of a circle $\mathcal{C}$ of radius $r = 0.338$. At

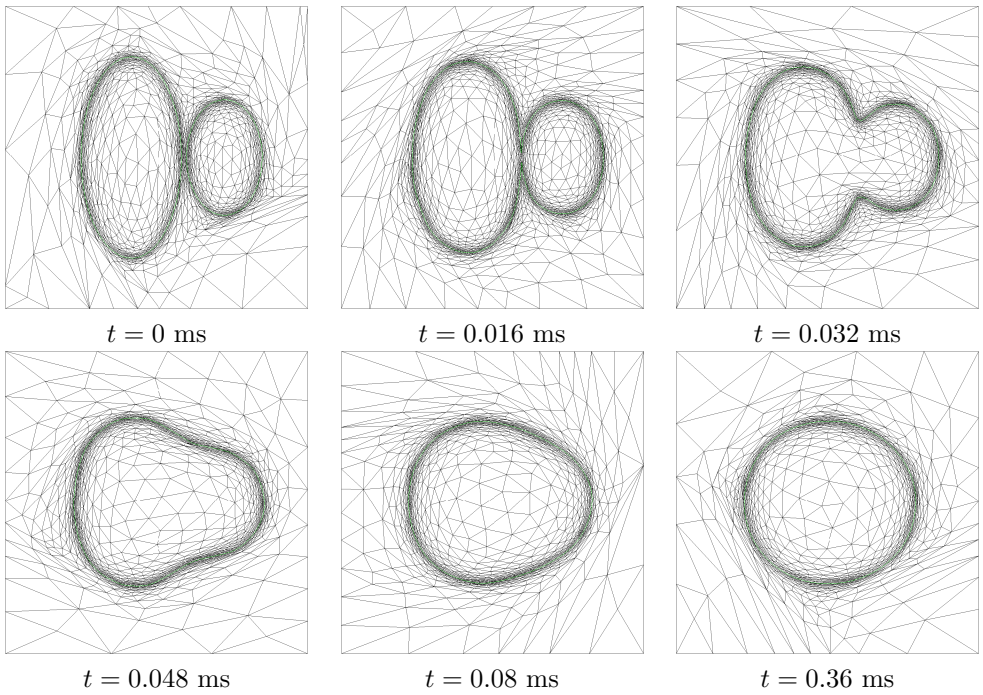

Figure 7. *Coalescence of droplets in zero gravity with a surface tension model: mesh adaptations. The green lines represent the interfaces.*

time $t = 0$, the center of gravity of two initial drops is located at $G_0(0.004097, 0)$. Hence, it is interesting to compare the final shape and location of the droplet to this circle $\mathcal{C}$. Figure 8 shows the final drop (in black) superimposed on the circle $\mathcal{C}$ of radius r (in green) centered at G_0. The final volume of the drop is $V = 0.348124$ and the loss of mass is $|V - V_0|/V_0 \approx 0.03$. We consider this value as acceptable since no specific mass loss control has been added to the advection resolution. Moreover, because of the piecewise affine approximation of the interface, there is always a mass loss in this evaluation. As there are no external force exerted on the system, the center of gravity must remain the same throughout the whole computation. Here, the center of gravity of the final drop is located at $G(0.002775, 0)$, the displacement being about 1.3×10^{-3} mm.

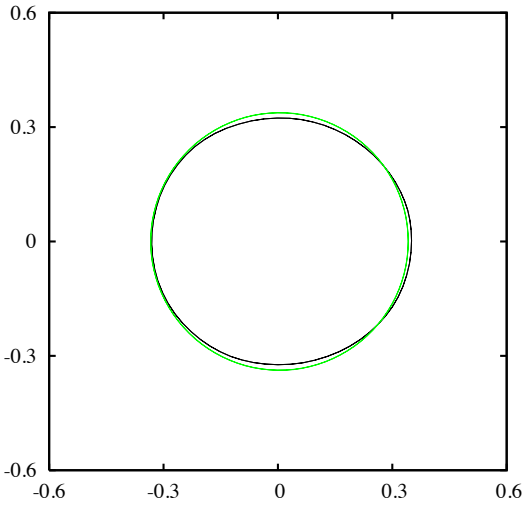

Figure 8. *Coalescence of droplets in zero gravity: final drop (black line) and reference disk (green line).*

3.3. Rising bubble

Finally, we have considered the rise of a gas bubble in a fluid under gravity and the coalescence of the bubble with its bulk phase. The computational domain is $\Omega = [0, 4] \times [0, 5]$ mm^2. The circular bubble is initially centered at $(2.0, 1.5)$, with a radius of 0.5 mm and the upper interface (hereafter called the surface) is the line $y = 3$ (cf. Figure 9, top left).

The density and the viscosity of the fluid are $\rho^1 = 100$ kg/m^3 and $\mu^1 = 10^{-1}$ kg/(m·s), respectively. The density and the viscosity of the gas are $\rho^2 = 1$ kg/m^3 and $\mu^2 = 10^{-2}$ kg/(m·s), respectively. The surface tension coefficient is quite small here, $\gamma = 6 \times 10^{-5}$ N/m. The gravity is set to $g = 9.81$ m/s^2. In the simulation, the problem is endowed with the following boundary conditions:

- homogeneous Dirichlet conditions, $\mathbf{u} = 0$, on the lower horizontal wall;
- free-slip condition on the vertical walls: $\boldsymbol{\tau} \cdot \sigma \cdot \mathbf{n} = 0$ and $\mathbf{u} \cdot \mathbf{n} = 0$;
- Neumann condition, $\sigma \cdot \mathbf{n} = 0$, on the top horizontal wall.

According to experimental results [1], the rising and coalescence process can be divided into three consecutive stages:

1. the *drainage* of the continuous film between bubble and bulk phases;
2. the *rupture* of the film and
3. the *growth* of the connection.

However, the comparison with these results may be difficult as the parameters are not the same in both cases. Nevertheless, a similar three-steps phenomenon is obtained in our simulation and the comparison curves of the surface position and evolution are in good accordance with the experimental data (cf. Figure 10).

Initially, both the bubble and the interface of the bulk phase are undistorted. The time step has been set to $\Delta t = 0.2$ s. We observe that the shape of the bubble as well as the surface become rapidly distorted (Figure 9, top center) and the deformations become even more pronounced until ultimately the rupture of the film occurs (Figure 9, top right). The velocity of the bubble slightly decreases with time. In Figure 10 (left), we represented the minimal distance h between the bubble and the upper surface (top), the distance between

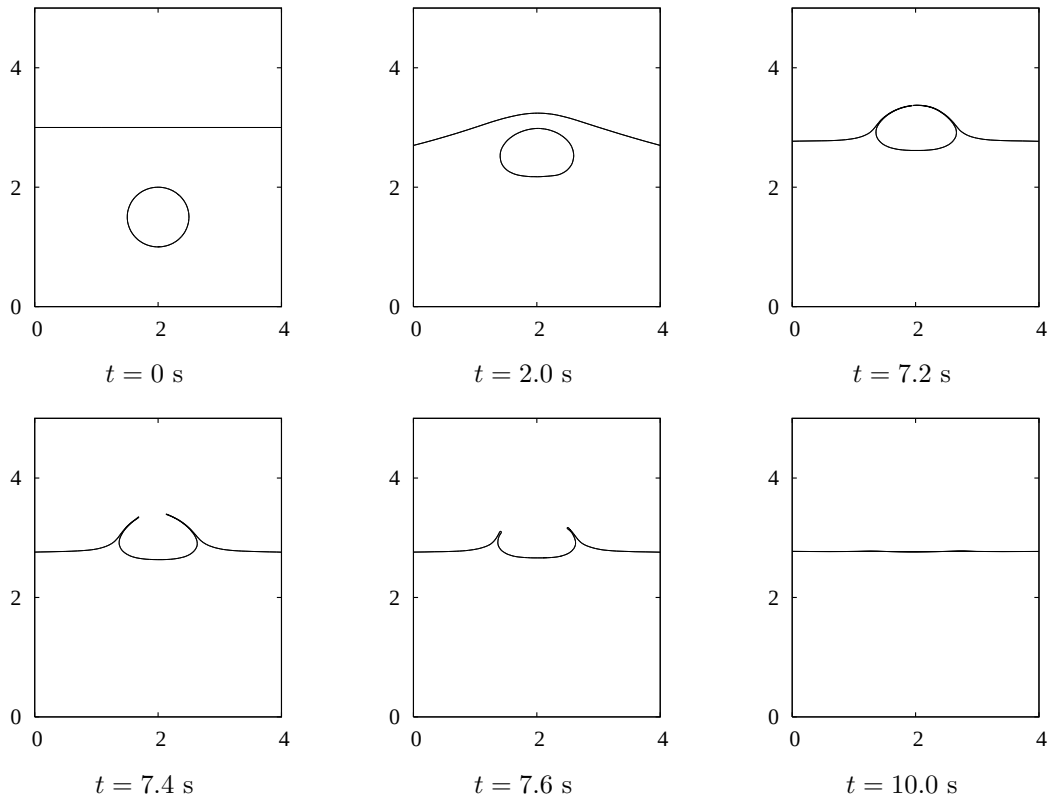

Figure 9. *Rising bubble: evolution of the interface in time. The coalescence occurs at* $t = 7.2$ *s and then the interface develops quickly.*

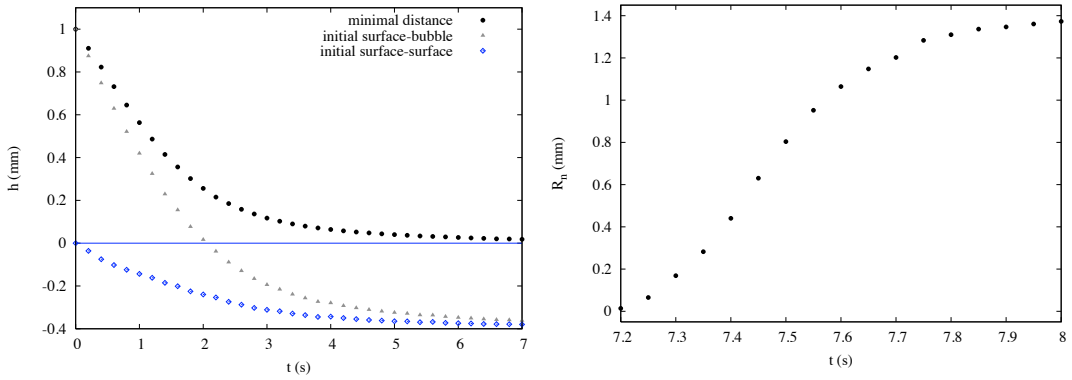

Figure 10. *Surface position as a function of time for the rising bubble (left). Diameter of the neck R_n as a function of time after the connection of the bubble and its bulk phase (right).*

the upper part of the bubble and the initial undistorted surface (middle), and the distance between the upper surface and the initial surface (bottom).

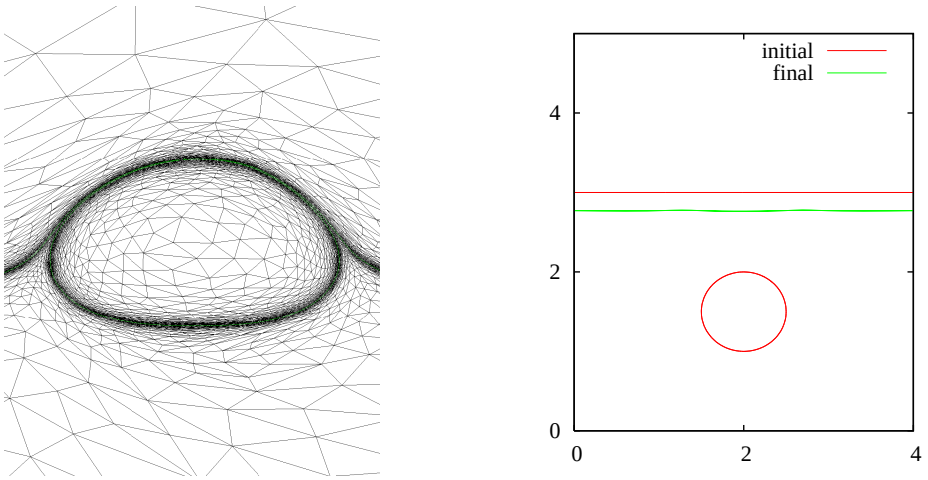

Figure 11. *Rising bubble: zoom on the computational mesh at the moment of coalescence $t = 7.2$ s (left) and the superposition of the initial and final interfaces (right).*

After the coalescence occured, the diameter of the neck R_n increases rapidly in time (cf. Figure 9, bottom), as the high local curvature close to the cusp points leads to a higher velocity in this region than in other part of the interface. This eventually forces to reduce the time step to $\Delta t = 0.01$ s. On Figure 10 (right), the curve shows that the diameter of the neck converges asymptotically to a limit value, the surface becoming then nearly flat. Figure 11 shows the mesh in the vicinity of the interface when the coalescence takes place and the initial and final volumes of the fluid.

REFERENCES

1. Aarts D., Lekkerkerker H., Droplet coalescence: drainage, film rupture and neck growth in ultralow interfacial tension systems, *J. Fluid Mech.*, 2008; **606**: 275-294.
2. Aksoylu B., Graham I.G., Klie H., Scheichl R., Towards a rigorously justified algebraic preconditioner for high-contrast diffusion problems, *Comput. Vis. Sci.*, 2008; **11**: 319-331.
3. Alauzet F., Frey P., Estimateur d'erreur géométrique et métriques anisotropes pour l'adaptation de maillage. Partie I: aspects théoriques, *preprint INRIA*, RR-4759, 2003.
4. Anderson D.M., McFadden G.B., Wheeler A.A., Diffuse-interface methods in fluid mechanics, *Annu. Rev. Fluid Mech.*, 1998; **30**: 139-165.
5. Apel T., *Anisotropic finite elements: local estimates and applications*, B.G. Teubner Stuttgart, Leipzig, Series of Advances in Numerical Mathematics, 1999.
6. Arrow K., Hurwicz L., Uzawa H., *Studies in Nonlinear Programming*, Stanford University Press, Stanford, 1958.
7. D'Azevedo E.F., Simpson R.B., On optimal triangular meshes for minimizing the gradient error, *Numer. Math.*, 1991; **59**: 321-348.
8. Babuška I., Aziz A.K., On the angle condition in the finite element method, *SIAM J. Numer. Anal.*, 1976; **13**: 214-226.
9. Barth T.J., Sethian J.A., Numerical schemes for the Hamilton-Jacobi and level set equations on triangulated domains, *J. Comput. Phys.*, 1998; **145**: 1-40.
10. Batchelor G.K., *An Introduction to Fluid Dynamics*, Cambridge University Press, 1967.
11. Borouchaki H., George P.L., Hecht F., Laug P., Saltel E., Delaunay mesh generation governed by metric specification: Part I. algorithms, *Finite Elem. Anal. Des.*, 1997; **25**: 61-83.
12. Bossen F.J., Heckbert P.S., A pliant method for anisotropic mesh generation, *Proc. 5th International Meshing Roundtable*, Sandia National Labs, Albuquerque, NM, 1996; 63-74.
13. Brackbill J.U., Kothe D.B., Zemach C., A continuum method for modeling surface tension, *J. Comput. Phys.*, 1991; **100**: 335-354.
14. Brezzi F., Fortin M., *Mixed and Hybrid Finite Element Methods*, Springer-Verlag, 1991.
15. Bui C., Frey P., Maury B., Méthode du second membre modifié pour la gestion de rapports de viscosité importants dans le problème de Stokes bifluide, *C. R. Mecanique*, 2008; **336**: 524-529.
16. Bui C., Frey P., Maury B., An accurate anisotropic adaptation method for solving the level set advection equation, submitted to *J. Comput. Phys.*, 2009.
17. Cahouet J., Chabard J.P., Some fast 3D finite element solvers for the generalized Stokes problem, *Int. J. Numer. Meth. Fluids*, 1988; **8**: 869-895.
18. Ciarlet P.G., *The Finite Element Method for elliptic problems*, Studies in Mathematics and its Applications, **4**, Elsevier, 1978.
19. Cuvelier C., Schulkes R.M., *Some numerical methods for the computation of capillary free boundaries governed by the Navier-Stokes equations*, D. Reidel Publishing Company, Dordrecht, 1986.
20. Dervieux A., Thomasset F., A finite element method for the simulation of a Rayleigh-Taylor instablity, in *Approximation Methods for Navier-Stokes problems*, Lecture Notes in Mathematics, 1980; **771**, Springer-Verlag, Berlin, 145-158.
21. Dobrzynski C., Frey P., Anisotropic Delaunay mesh adaptation for unsteady simulations, *Proc. 17th Int. Meshing Roundtable*, Sandia National Labs, Pittsburgh, PA, 2008; 177-194.
22. Donea J., Huerta A. , *Finite Element Methods for Flow Problem*, Wiley, 2003.
23. Dompierre J., Vallet M.G., Bourgault Y., Fortin M., Habashi W.G., Anisotropic mesh adaptation: towards user-independent, mesh-independent and solver-independent CFD. Part III: unstructured meshes, *Int. J. Numer. Meth. Fluids*, 2002; **39**: 675-702.
24. Ducrot V., Frey P., Anisotropic level set adaptation for accurate interface capturing, *Proc. 17th Int. Meshing Roundtable*, Sandia National Labs, Pittsburgh, PA, 2008; 159-176.
25. Elman, H.C., Golub, G.H., Inexact and preconditioned Uzawa algorithms for saddle point problems, *SIAM J. Numer. Anal.*, 1994; **31**(6): 1645-1661.
26. Enright D., Fedkiw R.P., Ferziger J., Mitchell I., A hybrid particle-level set method for improved interface capturing, *J. Comput. Phys.*, 2002; **183**: 83-116.
27. Formaggia L., Perotto S., New anisotropic a priori error estimates, *Numer. Math.*, 2001; **89**: 641-667.
28. Frey P., About surface remeshing, *Proc. 9th Int. Meshing Roundtable*, Sandia National Labs, New Orleans, LA, 2000; 123-136.
29. Frey P., A differential approach to mesh generation. In *Series in Contemporary Applied Mathematics*, P.G. Ciarlet, T. Li (eds), World Scientific, 2008.
30. Frey P., George P.L., *Mesh generation. Application to finite elements*, 2nd ed., Wiley, 2008.
31. Galusinski C., Vigneaux P., On stability condition for bifluid flows with surface tension: Application to microfluidics, *J. Comput. Phys.*, 2008; **227**: 6140-6164.

32. Garimella R.V., Shephard M.S., Boundary layer meshing for viscous flows in complex domain,*Proc. 7th Int. Meshing Roundtable*, Sandia National Labs, Albuquerque, NM, 1998; 107-118.
33. Girault V., Lopez H., Maury B., One time-step finite element discretization of the equation of motion of two-fluid flows, *Numerical Methods for Differential Equations*, 2006; **22**(3): 680-707.
34. Girault V., Raviart P.A., *Finite Element Methods for the Navier-Stokes Equations, Theory and Algorithms*, Springer-Verlag, Berlin, 1986.
35. Goldman R., Curvature formulas for implicit curves and surfaces, *Comp. Aided Geom. Design* 2005; **22**: 632-658.
36. Golub G.H., Van Loan C.F., *Matrix Computations*, The John Hopkins University Press, Baltimore and London, 3rd ed., 1996.
37. Harlow F.H., Welch J.E., Numerical calculation of time-dependent viscous incompressible flow of fluid with free surface, *Phys. Fluids*, 1965; **8**: 2182-2189.
38. Hecht F., Bidimensional anisotropic mesh generator, Technical Report, INRIA, RT-4759, 1997.
39. Huang H., Metric tensors for anisotropic mesh generation, *J. Comput. Phys.*, 2005; **204**: 633-665.
40. Loghin D., Wathen A.J., Analysis of preconditioners for saddle-point problems, *SIAM J. Sci. Comput.*, 2004; **25**(6): 2029-2049.
41. Löhner R., Cebral J., Generation of non-isotropic unstructured grids via directional enrichment, *Int. J. Numer. Methods Engng.*, 2000; **49**(1): 219-232.
42. Osher S., Fedkiw R.P., Level set methods: an overview and some recent results, *J. Comput. Phys.*, 2001; **169**: 463-502.
43. Osher S., Sethian J., Fronts propagating with curvature dependant speed: algorithms based on Hamilton-Jacobi formulations, *J. Comput. Phys.*, 1988; **79**: 12-49.
44. Peraire J., Vahdati M., Morgan K., Zienkiewicz O.C., Adaptive remeshing for compressible flow computations, *J. Comput. Phys.*, 1997; **72**: 449-466.
45. Pironneau O., *Finite Element Methods for Fluids*, John Wiley & Sons Inc, Chichester, UK, 1989.
46. Remacle J.F., Li X., Shephard M.S., Flaherty J.E., Anisotropic adaptive simulation of transient flows using discontinuous Galerkin methods, *Int. J. Numer. Meth. Eng.*, 2003; **62**(7): 899-923.
47. Renardy Y., Renardi M., PROST: a parabolic reconstruction of surface tension for the volume-of-fluid method, *J. Comput. Phys.*, 2002; **183**: 400-421.
48. Sethian J.A., *Level set methods and fast marching methods: evolving interfaces in computational geometry, fluid mechanics, computer vision and material science*, Cambridge University Press, U.K., 1999.
49. Shankar P.N., *Slow viscous flows*, Imperial College Press, 2007.
50. Shepel S.V., Smith B.L., On surface tension modelling using the level set method, *Int. J. Numer. Meth. Fluids*, 2009; **59**: 147-171.
51. Shin S., Juric D., Modeling three-dimensional multiphase flow using a level contour reconstruction method for front tracking without connectivity, *J. Comput. Phys.*, 2002; **180**: 427-470.
52. Shyy W., Udaykumar H.S., Rao M.M., Smith R.W., *Computational Fluid Dynamics with moving Boundaries*, Taylor & Francis, 1996.
53. Smolianski A., Numerical modeling of two fluid interfacial flows, PhD thesis, Jyväskylä University, 2001.
54. Sussman M., Smereka P., Osher S., A level set approach for computing solutions to incompressible two-phase flows, *J. Comput. Phys.*, 1994; **114**: 146-159.
55. Taubin G., A signal processing approach to fair surface design, in *Proc. ACM Siggraph*, 1995; **11**: 351-358.
56. Torres D.J., Brackbill J.U., The point-set method: front-tracking without connectivity, *J. Comput. Phys.*, 2000; **165**: 620-644.
57. Tryggvason G. et al., A front-tracking method for the computations of multiphase flow, *J. Comput. Phys.*, 2001; **169**: 708-759.
58. Yang X., James A.J., Lowengrub J., Zheng X., Cristini V., An adaptive coupled level-set/volume-of-fluid interface capturing method for unstructured triangular grids, *J. Comput. Phys.*, 2006; **217**: 364-394.
59. Yamakawa S., Shimada K., High quality anisotropic tetrahedral mesh generation via ellipsoidal bubble packing, *Proc. 9th Int. Meshing Roundtable*, Sandia National Labs, Albuquerque, NM, 2000; 263-273.
60. Zalesak S.T., Fully multi-dimensional flux corrected transport algorithms for fluid flow, *J. Comput. Phys.*, 1979; **33**: 335-362.